

Magnetic Properties and Environmental Temperature Effects on Battery Performance of $\text{Na}_{0.67}\text{Mn}_{0.5}\text{Fe}_{0.5}\text{O}_2$

Serdar Altin, Ali Bayri, Emine Altin, Erdinc Oz, Sedat Yasar, Sebahat Altundağ, Messaoud Harfouche, and Sevda Avci*

Herein, a modified solid state synthesis of $\text{Na}_{0.67}\text{Mn}_{0.5}\text{Fe}_{0.5}\text{O}_2$ and the results of a detailed investigation of the structural and magnetic properties via Fourier transform infrared spectroscopy (FTIR), X-ray diffraction (XRD), X-ray absorption spectroscopy (XAS), scanning electron microscopy (SEM), and energy dispersive X-ray (EDX) analysis are reported. The magnetic properties of $\text{Na}_{0.67}\text{Mn}_{0.5}\text{Fe}_{0.5}\text{O}_2$ do not fit the Curie–Weiss law and a model regarding the spin configuration of the Mn and Fe ions and a possible ferrimagnetic order is suggested. Electrochemical measurements and ex situ structural analysis of the cathode material confirm the reversible structural transitions for the cells charged up to 4.0 V. Environmental temperature-dependent electrochemical measurements reveal a strong temperature dependence of both, the initial capacity and the capacity retention. Ex situ SEM, FTIR, and XRD studies on the battery membrane verify the formation of a Na_2CO_3 phase on the membrane, which blocks the Na ion diffusion through membrane pores and is responsible for the capacity fade for this compound.

Layered Na_xTMO_2 (TM = transition metal) compounds have been the most heavily studied ones as cathode materials for Na-ion batteries because they are analogous to LiTMO_2 compounds and their energy densities are comparable to Li counterparts. These compounds may have two different layered structures: O3 and P2.^[1] O3 and P2 structures consist of TMO_2 slabs and Na ions that hold the octahedral and prismatic sites, respectively in between these slabs. O3-type materials usually have stoichiometric Na content such as $\text{NaNi}_{1/3}\text{Fe}_{1/3}\text{Mn}_{1/3}\text{O}_2$, $\text{NaFe}_{1/2}\text{Co}_{1/2}\text{O}_2$, and $\text{NaFe}_{1/2}\text{Mn}_{1/2}\text{O}_2$ and have lower reversible discharge capacity than P2-type compounds. In P2-type compounds, two-thirds of the Na sites are occupied by Na ions, for example, $\text{Na}_{2/3}\text{Co}_{1/3}\text{Mn}_{2/3}\text{O}_2$, $\text{Na}_{2/3}\text{Ni}_{1/3}\text{Mn}_{2/3}\text{O}_2$, and $\text{NaNi}_{1/3}\text{Mn}_{1/3}\text{Co}_{1/3}\text{O}_2$.^[2–4] There are two different Na

sites in the P2-type structure and three Na- sites in the O3-type structure.^[5] Such a difference in the crystal field of Na affects the redox potentials substantially.

P2-type $\text{Na}_{0.67}\text{Mn}_{0.5}\text{Fe}_{0.5}\text{O}_2$ is an important cathode material among the Na-based electrodes due to its high energy density (520 W h kg^{-1}), high capacity (190 mA h g^{-1}), and low cost, and its contents are environmentally benign. P2-type $\text{Na}_{0.67}\text{Fe}_{0.5}\text{Mn}_{0.5}\text{O}_2$ crystallizes in a hexagonal symmetry with space group $\text{P6}_3/\text{mmc}$ with lattice parameters $a = b = 2.9154 \text{ Å}$ and $c = 11.2599 \text{ Å}$. $\text{Na}_{0.67}\text{Fe}_{0.5}\text{Mn}_{0.5}\text{O}_2$ suffers from capacity fade attributed to the complex phase transitions during cycling.

1. Introduction

In the last decades, since the mobile electronic devices and electrical vehicles have come to prominence, the importance of rechargeable batteries has increased for energy storage. Although Li-based battery systems are dominant in the market, due to the shortage of Li resources, Na-based batteries have attracted attention. The natural abundance of Na, low toxicity, low cost, and similar intercalation chemistry to Li have made Na-ion batteries promising alternatives for Li-ion batteries.

Prof. S. Altin, Prof. A. Bayri, S. Altundağ
Physics Department
Inonu University
44280 Malatya, Turkey

Dr. E. Altin
IBTAM
Inonu University
44280 Malatya, Turkey

Dr. E. Oz
Department of Chemistry
Bilkent University
06800 Ankara, Turkey

Dr. S. Yasar
Chemistry Department
Inonu University
44280 Malatya, Turkey

Dr. M. Harfouche
Synchrotron-light for Experimental and Scientific Applications in the Middle East (SESAME)
P.O. Box 7, Allan 19252, Jordan

Dr. S. Avci
Department of Engineering Physics
Istanbul Medeniyet University
Istanbul 34700, Turkey
E-mail: sevda.avci@medeniyet.edu.tr

The ORCID identification number(s) for the author(s) of this article can be found under <https://doi.org/10.1002/ente.202001130>.

DOI: 10.1002/ente.202001130

However, early studies report that these phase transitions are all reversible even above 4.2 V.^[5,6] A very recent study by Wang et al. reports formation of a short-range nanosized ramsdellite phase in a highly disordered sample upon charging up to 4.5 V.^[7] They attribute the capacity loss to the formation of this ramsdellite phase. This detailed study clarifies the capacity loss mechanism very well if the cells are charged above 4 V. However, the capacity fade mechanism for the materials charged to 4 V and below is still undisclosed.

Herein, we report the synthesis and a thorough study of the structural, magnetic, and electrochemical properties of P2 Na_{0.67}Fe_{0.5}Mn_{0.5}O₂. We propose a ferrimagnetic order based on the spin configurations of Mn and Fe ions determined via magnetization measurements and X-ray absorption fine structure (XAFS) experiments. Regarding the electrochemical properties, first, via ex situ X-ray diffraction (XRD) and XAFS analysis we confirm the reversible structural transitions which cannot be held responsible for the capacity loss when the battery is cycled up to 4 V. Electrochemical measurements under various environmental temperatures reveal the strong environmental temperature dependence of the capacity retention behavior. We demonstrate the formation of a Na₂CO₃ phase on the membrane via ex situ scanning electron microscopy (SEM), XRD, and Fourier transform infrared spectroscopy (FTIR) data. We attribute the capacity loss to the formation of this Na₂CO₃ phase, which blocks the Na ion diffusion through the membrane.

2. Results and Discussion

2.1. Structural Properties

The XRD pattern shown in Figure 1a matches well with the reported structure of Na_{0.67}Fe_{0.5}Mn_{0.5}O₂ without any detected impurity phases within the resolution limits of our laboratory XRD device.^[8] The lattice parameters are determined from the Rietveld analysis as $a = b = 2.938364(233)$ Å and

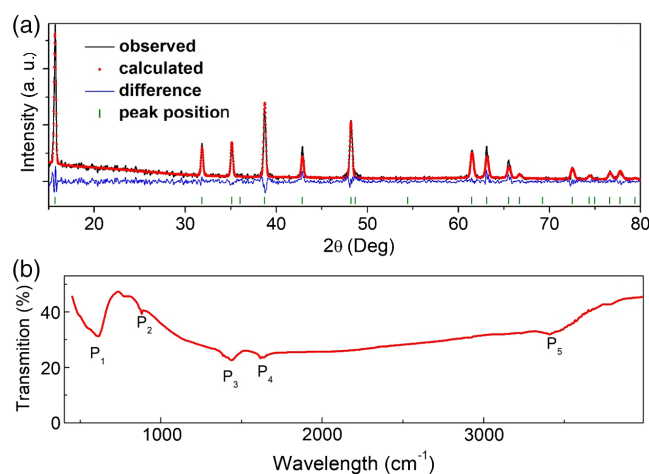


Figure 1. a) XRD pattern of Na_{0.67}Fe_{0.5}Mn_{0.5}O₂. Green tick marks, black solid lines, red dots, and blue solid lines represent the peak positions, observed intensities, calculated intensities, and the difference between the observed and calculated intensities, respectively. b) FTIR spectra of Na_{0.67}Fe_{0.5}Mn_{0.5}O₂. P₁, P₂, P₃, P₄, and P₅ point the peak positions.

Table 1. The FTIR peaks of Na_{0.67}Fe_{0.5}Mn_{0.5}O₂ and the corresponding bonds with related references.

Peak	Bond	Reference
P ₁	Fe—O bonds and Na—O bonds	[36,37]
P ₂	Fe—O	[38,39]
P ₃	Mn—O	[40]
P ₄	Fe—O	[41]
P ₅	Mn—O and Fe—O	[42]

$c = 11.18655(67)$ Å and are consistent with previously reported studies.^[9,10]

Figure 1b shows the FTIR spectra of Na_{0.67}Fe_{0.5}Mn_{0.5}O₂. The characteristic bands at 601 cm^{−1} (P₁ in Figure 1b) are related to the Fe—O bonds and bending Na—O bonds.^[11] The band at 874 cm^{−1} (P₂ in Figure 1b) is due to Fe—O—Fe^[12] and detailed information regarding the other peaks in the spectra are listed in Table 1. Proposed correlations between the electrochemical performance and the bond structures are discussed in the following sections.

2.2. Magnetic Properties

The valance states of the transition metal ions play a crucial role in the electrochemical properties of electrodes because the redox reactions and crystal fields of the Na ions have a strong dependence on them. The composition of Na_{0.67}Fe_{0.5}Mn_{0.5}O₂ can be expressed as Na_{0.67}¹⁺Fe_{0.5}^{3.33+}Mn_{0.5}^{3.33+}O₂[−] based on valance states of the elements and Mn and Fe ions share the same site. Both of these two ions can have 3+ and 4+ valance states. However, sharing of the same site by four different ions is possible only if the ligand field of that site is weak. Otherwise, a change in the valance state would distort the crystal structure, which prevents the other ions from settling in the same site. In the presence of a weak ligand field, the energy difference between e_{2g} and t_g is expected to be small so that the d electrons prefer to order as one electron at each orbital having the same spin due to the Pauli exclusion principle and Hund's rules.^[13] So, the transition metal ions are expected to have the following spin configurations. There is only one possibility for Mn⁴⁺ with three d -shell electrons with $S = 3/2$. Mn³⁺ ions are HS ($S = 2$), Fe³⁺ ions are HS ($S = 5/2$), and Fe⁴⁺ ions are HS ($S = 2$). Corresponding μ_{eff} values are calculated as $\sqrt{15}$, $\sqrt{24}$, $\sqrt{35}$, and $\sqrt{24}\mu_B$, for Mn⁴⁺, Mn³⁺, Fe³⁺, and Fe⁴⁺, respectively, using $\mu_{\text{eff}} = 2\sqrt{S(S+1)}$.

The literature on this material has a consensus regarding the existence of both Mn³⁺ and Mn⁴⁺ in this compound, which is reasonable due to the total valence of Mn being +3.33.^[10,14,15] However, there is some controversy regarding the valence of Fe ions. Park et al. report the existence of Fe²⁺ and Fe³⁺ ions via X-ray photo electron spectroscopy (XPS) analysis.^[2] Considering the charge balance, existence of Fe²⁺ ions would mean either oxygen deficiency in the composition or an unequal number of Mn and Fe atoms, which is not consistent with the composition. As a matter of fact, in Park et al.'s report, the provided atomic ratios of Fe²⁺/Fe³⁺ and Mn³⁺/Mn⁴⁺ ions require

oxygen deficiency to justify the charge balance. As a result, we rule out the existence of Fe^{2+} in $\text{Na}_{0.67}\text{Fe}_{0.5}\text{Mn}_{0.5}\text{O}_2$ composition. Park et al. via XPS analysis^[2] and Xu et al. via the Mössbauer spectroscopy technique^[10] claim the presence of only Fe^{3+} ions. This possibility requires a composition of $\text{Na}_{0.67}\text{Fe}_{0.5}(3+)\text{Mn}_{0.16}(3+)\text{Mn}_{0.33}(4+)\text{O}_2$. Here, we provide a thorough analysis of all the possibilities containing $\text{Mn}^{3+}/\text{Mn}^{4+}$ and $\text{Fe}^{3+}/\text{Fe}^{4+}$ and a clear evidence for the existence of both Fe^{3+} and Fe^{4+} based on the magnetization data.

Figure 2a shows the temperature-dependent magnetic susceptibility data of $\text{Na}_{0.67}\text{Mn}_{0.5}\text{Fe}_{0.5}\text{O}_2$ between 4 and 300 K. These data are consistent with the χ - T data in Xu et al.'s previous report^[10] and do not fit the Curie-Weiss law. The χ - T profile rules out the antiferromagnetic behavior as the magnetic susceptibility does not approach zero at 0 K. Ferromagnetic behavior is also a weak possibility as the susceptibility does not reach a saturation at low temperatures despite its increase with decreasing temperature. Such increase, however, is an indication of alignment of some spins in the same direction.

In the unit cell of $\text{Na}_{0.67}\text{Mn}_{0.5}\text{Fe}_{0.5}\text{O}_2$, Fe and Mn ions bond with each other through an oxygen bridge as $\text{Mn}-\text{O}-\text{Fe}$.^[16] The angle of these bonds has a crucial role for antiferromagnetic or ferrimagnetic/ferromagnetic behaviors^[16] as the superexchange and double-exchange interactions around the metal ions are directly related to the bridge structure of oxygen-metal-oxygen. The overlapping of the orbitals strongly depends on the angles.^[17] There are two possible magnetic interactions: same direction of the spins, which causes the ferromagnetic behavior, and opposite directions of the spins, which cause the antiferromagnetic or ferrimagnetic behavior. In ferromagnetic alignment, the magnetic moments of all the spins of the ions are expected to be equal, pointing in the same direction. In the antiferromagnetic behavior, the spins of different ions are expected to have equal magnetic moments pointing in opposite directions with zero net magnetic moment. In addition, the susceptibility is expected to decrease down to zero at 0 K below the Néel temperature. In ferrimagnetic behavior, spins of different ions can have different magnetic moments pointing in the same direction or opposite directions. Xu et al. report a ferromagnetic behavior in $\text{Na}_{0.67}\text{Mn}_{0.5}\text{Fe}_{0.5}\text{O}_2$ due to Mn^{3+} ions based on magnetic hysteresis.^[10] However, they completely disregard the magnetic contributions of Fe ions. In $\text{Na}_{0.67}\text{Mn}_{0.5}\text{Fe}_{0.5}\text{O}_2$, it is very unlikely for Mn and Fe ions to have equal spins pointing in the same direction. Therefore, we expect ferrimagnetic behavior

in $\text{Na}_{0.67}\text{Mn}_{0.5}\text{Fe}_{0.5}\text{O}_2$. In addition, lack of saturation of magnetization at high fields in Xu et al.'s magnetic hysteresis data does not support the ferromagnetic behavior. To confirm the ferromagnetic behavior further, we have performed a detailed analysis based on the possible valance state and ion ratio scenarios.

$$\begin{aligned} x(\text{Mn}^{3+}) + y(\text{Mn}^{4+}) &= 0.5 \\ z(\text{Fe}^{3+}) + t(\text{Fe}^{4+}) &= 0.5 \end{aligned} \quad (1)$$

where x , y , z , and t are the numbers of Mn^{3+} , Mn^{4+} , Fe^{3+} and Fe^{4+} ions in a formula unit of $\text{Na}_{0.67}\text{Fe}_z^{3+}\text{Fe}_t^{4+}\text{Mn}_x^{3+}\text{Mn}_y^{4+}\text{O}_2$ composition, respectively. These numbers must be multiplied by the Avagadro's number to obtain the actual number of atoms in 1 mole of material. Based on the charge equilibrium condition, a series of equations can be obtained that do not have a trivial analytical solution. To understand the real state in the sample, let us consider a liner system with only 12 transition metal atoms. The equations take the form

$$\begin{aligned} y + t &= 4 & x + y &= 6 \\ x + z &= 8 & z + t &= 6 \end{aligned} \quad (2)$$

Possible solutions to these equations are

x (Mn^{3+})	y (Mn^{4+})	z (Fe^{3+})	t (Fe^{4+})
2	4	6	0
3	3	5	1
4	2	4	2
5	1	3	3
6	0	2	4

There are five different solution sets and when we draw the possible solution set as one layer, a 12×5 matrix is obtained, as shown in Figure 2b. The μ_{eff} values of all ions for trigonal environment and corresponding magnetic ordering types are also shown in Figure 2b. Although the modeled solutions are only based on 12 individual metal ions, when the number of ions is increased, the even coefficients show an antiferromagnetic order and odd coefficients show ferrimagnetic order with the average μ_{eff} value greater than zero due to ferrimagnetic order. As the temperature-dependent susceptibility data confirm the ferrimagnetic behavior, we conclude that the material has all four Fe^{3+} , Fe^{4+} , Mn^{3+} , and Mn^{4+} ions with second or fourth

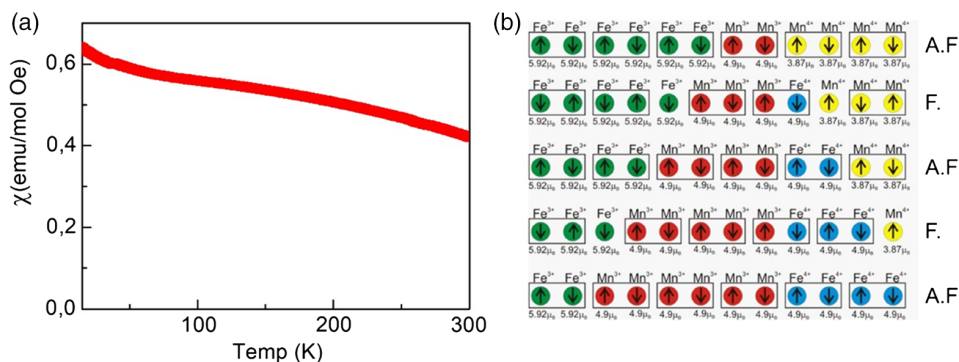


Figure 2. a) χ - T measurement of $\text{Na}_{0.67}\text{Fe}_{0.5}\text{Mn}_{0.5}\text{O}_2$ and b) suggested spin configuration.

possibility. In other words, the composition can be written as either $\text{Na}_{0.67}\text{Fe}_{5/12}(3+)\text{Fe}_{1/12}(4+)\text{Mn}_{1/4}(3+)\text{Mn}_{1/4}(4+)\text{O}_2$ or $\text{Na}_{0.67}\text{Fe}_{1/4}(3+)\text{Fe}_{1/4}(4+)\text{Mn}_{5/12}(3+)\text{Mn}_{1/12}(4+)\text{O}_2$ with dominantly ferrimagnetic behavior. Such ferromagnetic order is expected to suppress the octahedral distortions and contribute to the structural stability of $\text{Na}_{0.67}\text{Mn}_{0.5}\text{Fe}_{0.5}\text{O}_2$ upon cycling.^[18,19]

2.3. Electrochemical Performance

The cyclic voltammetry (CV) curves of $\text{Na}_{0.67}\text{Mn}_{0.5}\text{Fe}_{0.5}\text{O}_2$ between 1.5 and 4.0 V at different scanning rates are shown in Figure 3a. In these curves, there are two anodic and two cathodic peaks,^[2,10] which are more pronounced in the slow scan rate measurement in Figure 3a. Low-potential and high-potential peaks represent the $\text{Mn}^{3+}/\text{Mn}^{4+}$ and $\text{Fe}^{3+}/\text{Fe}^{4+}$ redox reactions, respectively. As the sweep rate increases, the peaks get broader and the area of the curves increases because faster scan rates shorten the diffusion paths.^[20,21] It is possible to calculate the diffusion coefficient of the Na ions by using the Randles–Sevcik equation as

$$I_p = 2.69 \times 10^5 n^{3/2} A D_{\text{Na}}^{1/2} C_{\text{Na}} \nu^{1/2} \quad (3)$$

where I_p is the peak current, n is the number of electrons, A is the surface area, D is the diffusion coefficient of Na^+ ions, C_{Na} is the concentration of Na ions in the cathode, and ν is the scan rate. Peak currents versus the square root of the scan rate plot (presented in Figure 3b) provide valuable information regarding the diffusion of Na ions. A linear plot is an indication of freely diffusing Na ions, whereas any deviations from linearity suggest either electrochemical quasi-reversible processes or the surface adsorption of Na ions on electrodes.^[20] The slope of the linear plot (Figure 3b) gives the diffusion coefficient of the Na ions, which is calculated as $D = 4.08 \times 10^{-12} \text{ cm}^2 \text{ s}^{-1}$. There are inconsistent diffusion coefficient values in the literature.^[8,14] However, Bai et al. report a significant variation in the diffusion coefficient values upon changes in the sol–gel synthesis conditions (temperature and ingredients) of $\text{Na}_{0.67}\text{Mn}_{0.5}\text{Fe}_{0.5}\text{O}_2$.^[22] Thus, it is expected to obtain different values for different synthesis techniques.

The main panel of Figure 4a shows the capacity versus cycle number and the inset shows the galvanostatic charge/discharge measurement profiles up to 100 cycles at C/3 rate. The voltage window of the galvanostatic cycling is chosen as 1.5–4.0 V. Two apparent voltage plateaus in the charge–discharge profiles corresponding to $\text{Mn}^{3+}/\text{Mn}^{4+}$ and $\text{Fe}^{3+}/\text{Fe}^{4+}$ redox couples are pronounced. Charge/discharge capacities decrease with increasing

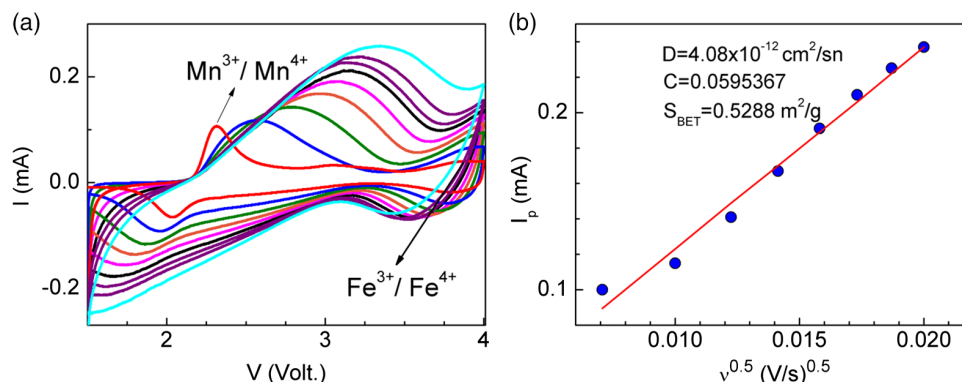


Figure 3. a) Cyclic voltammogram curves of $\text{Na}_{0.67}\text{Mn}_{0.5}\text{Fe}_{0.5}\text{O}_2$ under various scan rates (from 0.05 mV s^{-1} (red) to 0.5 mV s^{-1} (cyan) with 0.05 mV s^{-1} intervals). b) I_p versus $\nu^{1/2}$ graph (here, the low-voltage oxidation peak is considered). The data were collected at room temperature.

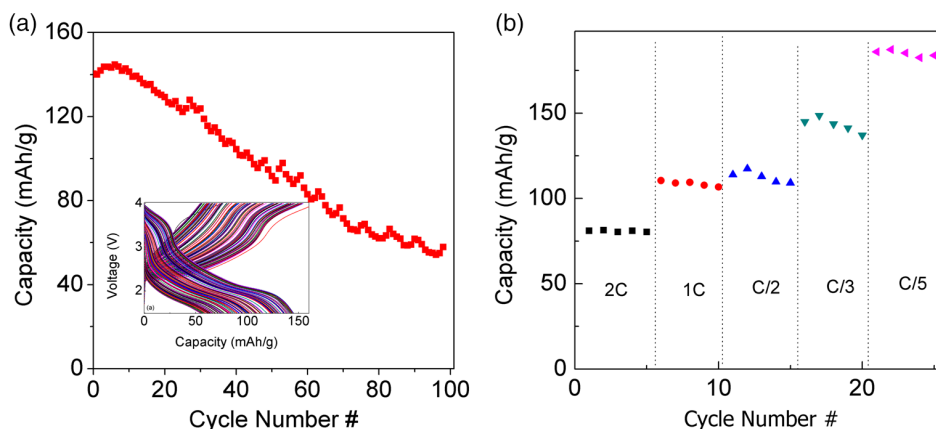


Figure 4. a) Capacity versus cycle number for 100 cycles at C/3 rate. The inset shows the capacity–voltage profiles. b) Cycling performance of the cell cycled at different C rates. Both measurements are performed in the voltage window of 1.5–4.0 V.

cycle number and the battery loses 60% of its initial capacity at the end of 100 cycles. Such capacity loss has been reported for this compound for the cycle measurements collected between the voltage window of 1.5 and 4.2 V^[22,23] and above 4.0 V.^[2,10,24] Capacity loss when the battery is cycled with a cut-off voltage of above 4.2 V is attributed to the formation of a segregated short-range nanosized ramsdellite phase in the highly desodiated electrode, which is an irreversible process confirmed via neutron powder diffraction and neutron pair distribution function analysis. In contrast, all the phase transitions when the cycling cut-off voltage is 4.2 V or below are reported as reversible.^[5,6] However, the mechanism for the capacity loss despite reversible phase transition in this voltage window has not been addressed clearly.

The rate performance of $\text{Na}_{0.67}\text{Mn}_{0.5}\text{Fe}_{0.5}\text{O}_2$ in the 1.5–4.0 V voltage range at different current rates of $C/5$, $C/3$, $C/2$, C , and $2C$ is shown in Figure 4b. As the current rate decreases, the capacity increases gradually from 80 mA h g^{-1} at $2C$ to 180 mA h g^{-1} at $C/5$. Such a difference is expected. The effect of the C rate on capacity is related to the overpotential (dissipated energy) associated with the concentration polarization phenomenon in the electrode. Concentration polarization is a result of faster consumption of the reactant at high current loads than its diffusion rate into the electrode. The overpotential is expected to be high at high C rates, which reduces the chemical potential difference between the electrodes and the amount of transferred ions.^[25–27]

One of the important factors affecting the battery performance of rechargeable batteries is the temperature of their environment. Na-ion batteries have prospective usage for storing energy generated by renewable energy sources. These sources usually require outdoor storage units that are exposed to a range of temperature environments. To understand the temperature environment effects on battery performance, we have performed galvanostatic cycling measurements at 10–50 °C using an EN-120 incubator. Figure 5a,b shows the galvanostatic charge–discharge profiles for the 1st, 25th, 50th, and 100th cycles at 10 and 50 °C, respectively. The two voltage plateaus that are visible in the

first cycles at both temperatures are clear indication that both electrochemical redox reactions ($\text{Mn}^{3+}/\text{Mn}^{4+}$ and $\text{Fe}^{3+}/\text{Fe}^{4+}$) proceed at both temperatures. However, these plateaus fade away and the capacity decreases abruptly by the 25th cycle under 50 °C temperature environment. It is a clear conclusion that some irreversible transitions occur that hinder the redox reactions and reduce the capacity at this temperature. A profound effect of environmental temperature on the cycling properties of the cells can be seen clearly in Figure 5c. Initial capacities are high as $\approx 155 \text{ mA h g}^{-1}$ for 40 and 50 °C measurements. We attribute such a high initial capacity at 40 and 50 °C to the temperature dependence of the chemical reaction and diffusion rates.^[28] However, capacity retention capabilities are very weak as the battery loses $\approx 85\%$ of its initial capacity by the 20th cycle under a 50 °C temperature environment. In contrast, the measurements at 10 and 20 °C show better capacity retention properties than the measurements at 30, 40, and 50 °C despite their lower initial capacities.

To understand further the effect of the environmental temperature on the battery performance, we performed several ex situ measurements as presented subsequently in detail.

2.4. Ex Situ Cathode Study

The XRD pattern of the coated electrode is shown in Figure 6a. All of the peaks are assigned to $\text{Na}_{2/3}\text{Mn}_{0.5}\text{Fe}_{0.5}\text{O}_2$ with a broad halo around 20° which is due to the additives in the electrodes. Ex situ XRD patterns of the electrodes that are cycled at 10–50 °C for 100 cycles are also shown in Figure 6a. Some impurity phases are determined such as MnO_2 , Fe_2O_3 , $\text{Na}_{0.7}\text{MnO}_2$, Fe_3O_4 , and MnO as shown in the figure.

We have also collected XRD data on electrodes that were cycled up to 5, 10, 20, and 100 cycles at 50 °C. The observed impurity phases in the electrodes cycled at 50 °C are the same as those of the electrodes cycled at different environmental temperatures up to 100 cycles. Although the impurity phases in the cathode surely affect the battery performance, we expect other factors to contribute to the capacity fade because the capacity values after 100

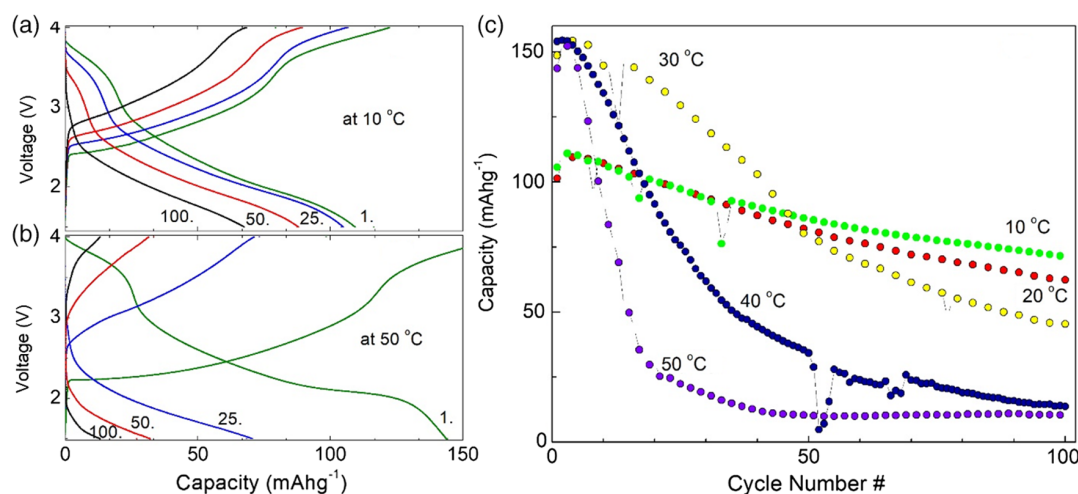


Figure 5. Galvanostatic charge–discharge profiles at a) 10 °C, b) 50 °C, and c) capacity versus cycle number under various environmental temperatures at $C/3$ rate.

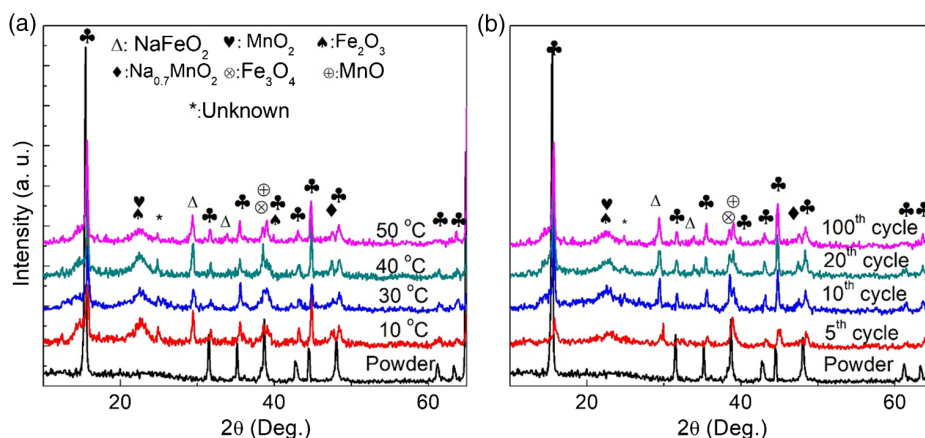


Figure 6. Ex situ XRD of the electrode a) under different environmental temperatures after 100 cycles and b) after different cycle numbers at 50 °C at C/3 rate.

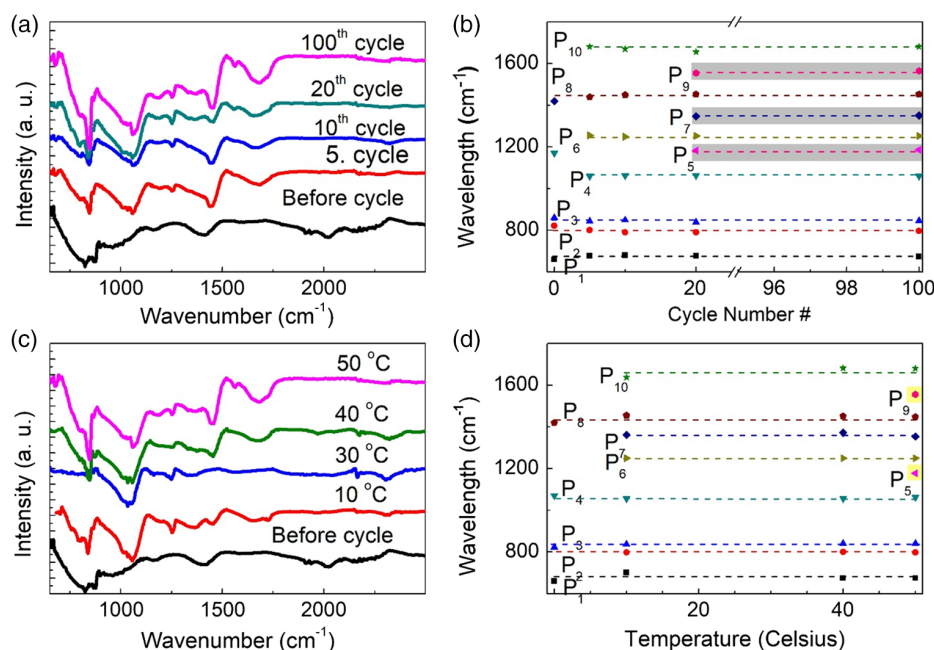


Figure 7. Ex situ FTIR for a) different cycle numbers at 50 °C and b) their peaks and c) different environmental temperatures and d) their peaks.

cycles are significantly different for the batteries cycled below and above 30 °C.

The change in the bond structure of the electrodes is also important for revealing the capacity fade mechanism of the cells. First, we measured the FTIR spectra of the electrodes before and after cycling at different temperatures, as shown in Figure 7a. The peaks in the FTIR spectra and the corresponding bonds belong to the electrodes and the components along with the

related references are listed in Table 2. The P₁, P₂, P₃, P₄, and P₈ peaks displayed in Figure 7b are present both in the unprocessed electrode and in the cycled electrodes. The P₅ and P₉ peaks are present only in the FTIR spectrum of the 100 cycle electrode at 50 °C. Increasing capacity fade with increasing temperature may be caused by this particular structural modification. To test this speculation, we performed ex situ FTIR measurements on cathodes after 5–100 cycles at 50 °C, as

Table 2. The bonds and related references in ex situ FTIR spectra of cathodes.

FTIR peaks	P ₁	P ₂	P ₃	P ₄	P ₅	P ₆	P ₇	P ₈	P ₉	P ₁₀
Bond	CH	CH	CH, CO, C–Cl, Na	CH, COH, CN, CO	CF ₂	CO	COH	CO, CH ₃	CO	OH, CO
Reference	[43]	[44]	[45–48]	[44,49–51]	[52,53]	[54,55]	[49]	[45,56]	[57]	[58]

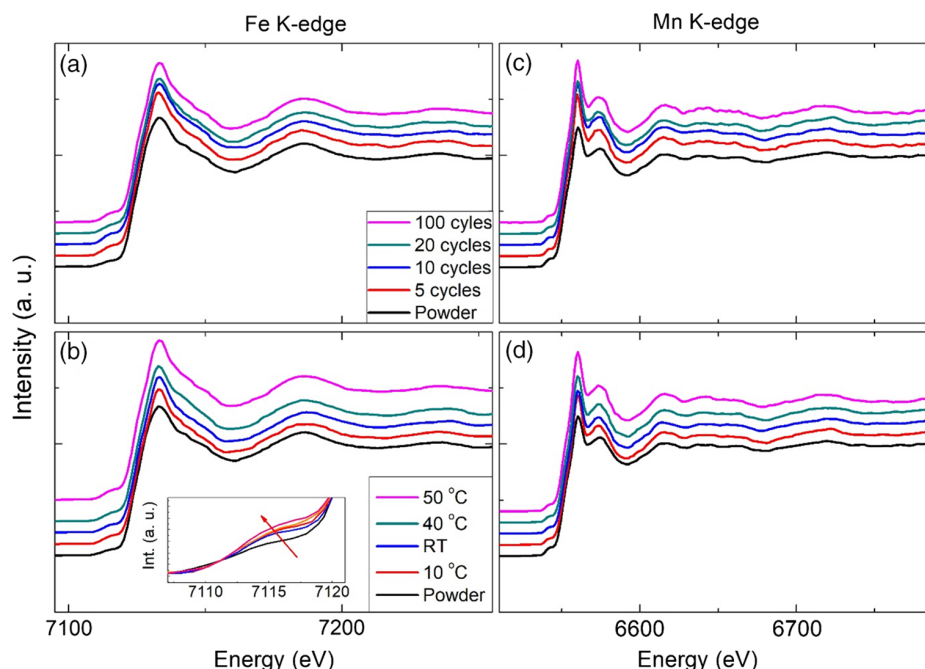


Figure 8. Ex situ Fe K-edge XANES for a) different cycle numbers at 50 °C, b) different environmental temperatures after 100 cycles and Mn K-edge for c) different cycle numbers at 50 °C, d) different environmental temperatures after 100 cycles. Legends in (a) and (b) are valid for (c) and (d), respectively.

shown in Figure 7c. We observed the presence of these two peaks after the tenth cycle.

To understand the relation between the capacity fade mechanism and the valence state changes upon cycling and the increasing temperature, we measured X-ray absorption near edge structure (XANES) spectra at the K-edges of Mn (6539 eV) and Fe (7112 eV) as shown in Figure 8a–d. The ex situ XANES measurements were performed for 100 cycled cells at 10–50 °C and 5, 10, 20, and 100 cycle cells in a 50 °C temperature environment.

XANES Fe K-edge spectra of unprocessed $\text{Na}_{0.67}\text{Fe}_{0.5}\text{Mn}_{0.5}\text{O}_2$ powders show the existence of Fe^{3+} and Fe^{4+} and there is no sign of Fe^{2+} , as shown in Figure 8b. XANES spectra at the K-edge of Fe for the cells cycled at 10–50 °C show almost identical features to the spectrum of the unprocessed powder (Figure 8a). This is a clear indication that the valence state of Fe does not change with increasing temperature (based on the derivative of the XANES spectra).

Similarly, XANES spectra at the Fe K-edge of the 5, 10, 20, and 100 cycle cells under 50 °C temperature exhibit similar features, as shown in Figure 8b. This is a clear indication that the Fe ions are stable during repeated cycling. The XANES spectra collected at Mn K-edge for different environmental temperatures and different cycles at 50 °C are shown in Figure 8c,d. These spectra also show that Mn ions remain unchanged upon cycling and increasing temperature. Although there are some impurity phases in ex situ XRD data of the cathodes, we have not observed any significant changes in the valence states of the transition metals with increasing cycle number and temperature.

Fourier transform (FT) of Fe and Mn extended X-ray absorption fine structure (EXAFS) at K-edges for the unprocessed and 100 cycle cathode at different environmental temperatures and different cycles at 50 °C are shown in Figure 9. Merelli et al. state that the first peaks correspond to Fe/Mn–O bonds in

$\text{Na}_{0.67}\text{Fe}_{0.5}\text{Mn}_{0.5}\text{O}_2$ and the second peaks are due to Fe/Mn–Fe/Mn bonds.^[29] The kink around 1.1 Å in Figure 9a,b may be due to the formation of Fe-impurity phases in the structure. A similar kink is present in Mn K-edge spectrum, as shown in Figure 9c,d. The parameters obtained from the Fourier transform of the EXAFS data are listed in Table 3. A detailed inspection shows that interatomic distances do not change significantly upon cycling, which is a clear indication of structural stability.

2.5. Ex Situ Membrane Properties

After ruling out possible structural modifications regarding the origins of fast capacity fade in $\text{Na}_{0.67}\text{Fe}_{0.5}\text{Mn}_{0.5}\text{O}_2$, we decided to pursue a new approach, which is based on investigating the deformations in membrane upon cycling and increase in temperature. The most popular membranes for Na-ion batteries are glass fiber membranes such as Whatman GF/D, GF/B, nylon membrane, and polytetrafluoroethylene (PTFE) membranes. The main problem of the membranes in Na-ion battery cells is the ionic radius of Na (>0.99 Å), which is larger than Li ions (≈0.6 Å). Therefore, developing new membranes for Na-ion batteries is a challenging issue. As stated earlier, Whatman GF/D is used as a membrane in this study and we have investigated the structural and morphological properties of the membrane after cycling at different environmental temperatures. Figure 10a shows the surface morphology of the Whatman GF/D membrane that has randomly oriented glass fibers (detailed properties of this membrane can be found in a previous study^[30]). One surface of the membrane interacts with the anode and the other surface interacts with the cathode. We have studied the morphology of the membrane surface to understand its roles in the capacity fade of the cells upon temperature increase (Figure 10b–d).

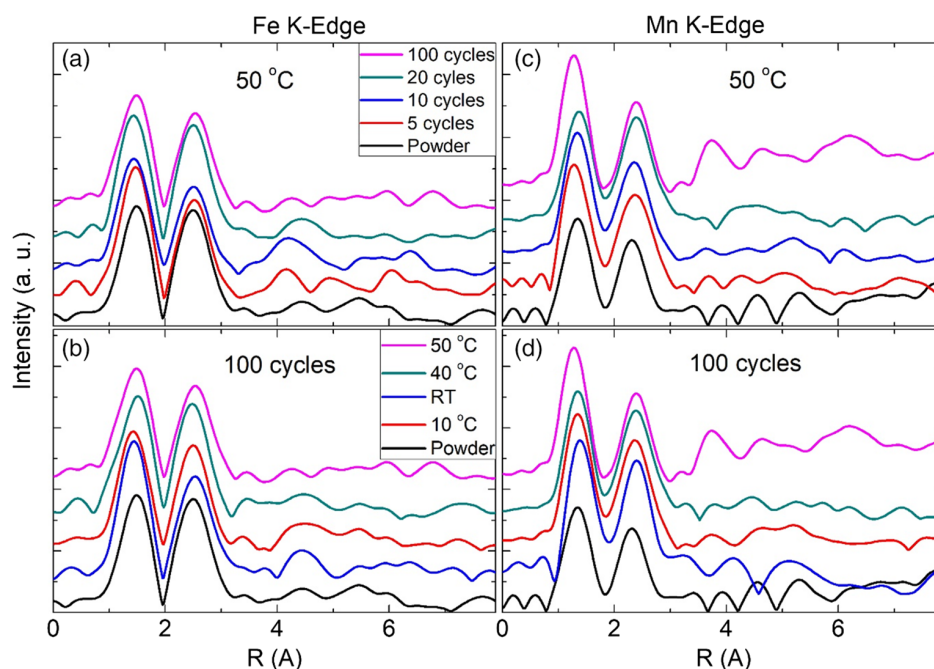


Figure 9. FT of the k^2 -weighted EXAFS signal collected at the Fe K-edge for a) different cycle numbers at 50 °C, b) different environmental temperatures after 100 cycles and at the Mn K-edge for c) different cycle numbers at 50 °C, d) different environmental temperatures after 100 cycles. Legends in (a) and (b) are valid for (c) and (d), respectively.

Table 3. Structural parameters from FT of EXAFS spectra. Number of backscattering atoms N , interatomic distance R , Debye–Waller factor σ^2 , and the inner potential shift ΔE are listed.

Sample	Bond	N	R [Å]	σ^2 [Å ²]	ΔE [eV]
<i>Fe-K-edge</i>					
Unprocessed powders	Fe—O	3.7 (3)	2.000 (5)	0.0020 (1)	3.88 (1)
	Fe—Fe	6.6 (1.0)	2.930 (4)	0.0074 (1)	
100 cycles at room temperature	Fe—O	4.4 (3)	1.990 (4)	0.0026 (1)	3.71 (4)
	Fe—Fe	5.6 (7)	2.930 (5)	0.0062 (1)	
100 cycles at 50 °C	Fe—O	5.0 (2)	2.010 (2)	0.0070 (7)	3.85 (5)
	Fe—Fe	6.2 (4)	2.940 (1)	0.0080 (8)	
<i>Mn K-edge</i>					
Unprocessed powders	Mn—O	3.5 (1)	1.900 (8)	0.005 (1)	0.50 (8)
	Mn—Mn	3.8 (9)	2.920 (9)	0.0050 (3)	
100 cycles at room temperature	Mn—O	3.9 (1)	1.860 (4)	0.0005 (1)	−1.87 (6)
	Mn—Mn	5.7 (1.0)	2.870 (8)	0.009 (2)	
100 cycles at 50 °C	Mn—O	4.1 (1)	1.880 (1)	0.0030 (4)	0.29 (2)
	Mn—Mn	4.9 (1)	2.920 (3)	0.004 (1)	

There are some materials stacked to the anode side surface of the membrane for the samples with 100 cycles at 10 °C and 10 cycles at 50 °C where the inner part of the membrane shows a porous structure similar to the unprocessed membrane. Similarly, the surface structures of the cathode interface of the membrane maintain their properties. We suppose that the stacked materials on the membranes are due to the SEI layer and consist of Na-based compositions.

The changes for both sides of the membrane surface structure after 100 cycles at 50 °C are shown in Figure 10d. These SEM

images are a clear clue about the change of the chemical structure of the fiberglass in the membranes and the disappearance of the pore structure. It is clear that the loss of permeability of the membrane has a profound effect on the battery performance and we propose that the fast capacity fade in our batteries upon repeated cycling and increasing temperature is due to the deformations in the membrane. To further confirm this statement, we performed elemental dot mapping for 100 cycle cells at 10 and 50 °C as shown in Figure 11a,b, respectively. We observed the presence of Na, Cl, Fe, and Mn ions in the anode surface of the membrane, although

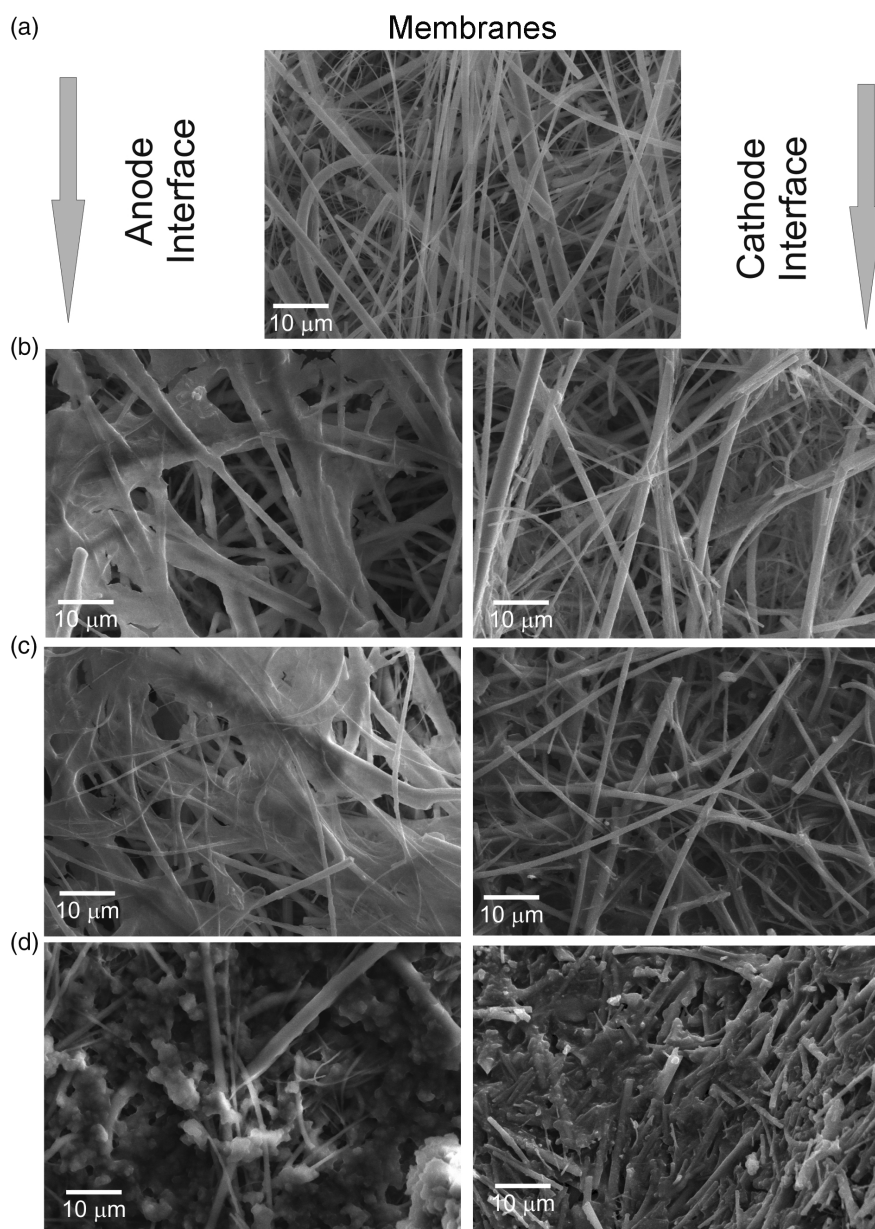


Figure 10. SEM images of membrane a) before cycling and after b) 100 cycles at 10 °C, c) 10 cycles at 50 °C, and d) 100 cycles at 50 °C.

the EDS counts of Mn and Fe are very low compared to the other elements. So, the anode side surface consists of mainly Na and Cl ions. The sources of the Na ions are the anode, cathode, and electrolyte and Cl ions are present only in the electrolyte. Although we washed the membrane thoroughly with deionized water before the measurements, it is possible that some of the electrolyte could not be totally removed from the surface.

XRD and FTIR measurements of the membrane were performed to identify the unwanted chemical structures, as shown in **Figure 12a,b**. The unprocessed membrane exhibits amorphous structure, which gives a broad halo around 25° as there is short-range order in the structure. Although there are no crystalline peaks for the cycled membrane at 10 °C, XRD peaks of Na₂CO₃

were obtained for the membranes cycled at 40 and 50 °C. The FTIR spectra of the unprocessed and cycled membranes are shown in **Figure 12b** and the peak values are displayed in **Table 4**. The ex situ FTIR spectra of the membranes have two groups of peaks: One is observed upon cycling without the environmental temperature. This is classified as the yellow-colored region in the spectra. The second group of peaks, shown as the turquoise-colored region, is observed in the spectra of the cells cycled at 40 and 50 °C, which show the highest capacity fade. We suggest that this second group of peaks causes the degradation of the cells.

The Whatman membranes are fabricated using borosilicate glass and the main peak of the FTIR spectra in this study is due to BO₄ at 1031 cm⁻¹.^[31] When the battery is cycled, the peaks

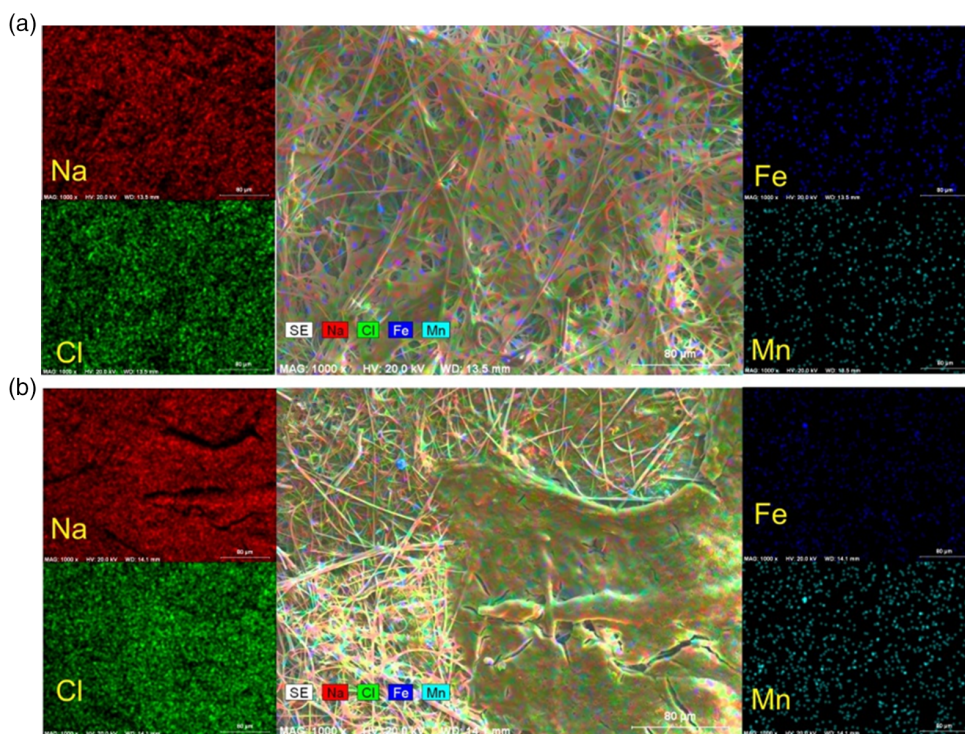


Figure 11. EDS dot mapping of membrane after 100 cycles at a) 10 °C and b) 50 °C.

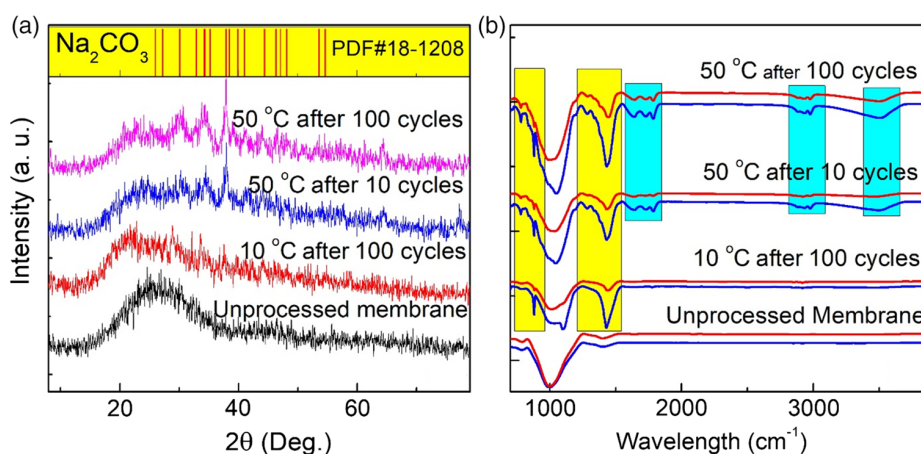


Figure 12. Ex-situ a) XRD patterns and b) FTIR spectra of membrane, for each pair of spectra at different conditions; top (red) and bottom (blue) solid lines represent the anode and cathode interfaces, respectively.

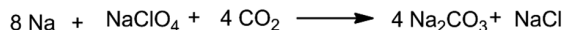
Table 4. The FTIR peaks and corresponding bonds.

FTIR peaks	777	887	1031	1437	1636	1714	1787	2906	2980	3510
Bond	Si—C	Na ₂ CO ₃	BO ₄	Na ₂ CO ₃ C—O CH ₂	ClO ₄ —	C = O	Na ₂ CO ₃	Na ₂ CO ₃	O—H	O—H
Reference	[59]	[60]	[31]	[60–63]	[64]	[63]	[61]	[61]	[65]	[66]

belonging to Na₂CO₃,^[32] Si—C, and C—O and CH₂ bonds are present for all environmental temperatures. The turquoise-colored region of peaks is due to ClO₄[−], C=O, O—H, and NaClO₄ phases. Although the Na₂CO₃ crystalline phase is

observed for the cathode cycled at 40 and 50 °C in XRD measurements, the FTIR peaks reveal that the Na₂CO₃ phase starts appearing upon cycling. Based on this finding, we suggest the subsequent reaction chain which confirms the formation of

Na_2CO_3 after each cycle, which adversely affects the battery performance specifically accumulating at high cycle numbers.



The ethylene carbonate (EC) and propylene carbonate (PC) are shown as CO_2 source in the proposed reactions. In the literature, CO_2 release has been reported as a result of degradation of EC and PC.^[33] Thus, we suggest that the C=O, O–H peaks should be due to PC and fluoroethylene carbonate (FEC) in the electrolyte and the Na_2CO_3 content in the membrane has a crucial role in the battery performance.

3. Conclusion

We report the successful synthesis of $\text{Na}_{0.67}\text{Mn}_{0.5}\text{Fe}_{0.5}\text{O}_2$ by quenching at high temperature. Its structural properties show that the phase is pure and there are no impurity phases in the structure within the detection limits of our device. The temperature dependence of magnetic susceptibility does not obey the Curie–Weiss law. We present a detailed analysis of the possible valence states of the transition metal ions and propose ferromagnetic behavior based on magnetization data and valence state analysis. We have confirmed the valence states via X-ray absorption spectroscopy measurements. CV measurements with different scan rates enabled us to determine the diffusion rate of the Na ions. From the literature it is known that $\text{Na}_{0.67}\text{Fe}_{0.5}\text{Mn}_{0.5}\text{O}_2$ has reversible reactions when cycled below 4.0 V. However, its capacity still fades upon repeated cycling. Its performance under various environmental temperatures has not been investigated also. First of all, we investigated the battery performance of $\text{Na}_{0.67}\text{Fe}_{0.5}\text{Mn}_{0.5}\text{O}_2$ at 10, 20, 30, 40, and 50 °C and found that capacity fades faster at 40 and 50 °C than it does at lower temperatures, although the initial capacities are higher for 40 and 50 °C measurements. Second, we confirmed the structural stability upon repeated cycling and at various temperatures via ex situ characterization techniques such as XRD, XAS, and FTIR. Then, we developed a new approach to investigate the capacity fade mechanism by examining the membrane, which plays a crucial role during cycling. Ex situ SEM, EDX, XRD, and FTIR data confirm the formation of Na_2CO_3 on the membrane surface, which is attributed to the capacity fade of $\text{Na}_{0.67}\text{Fe}_{0.5}\text{Mn}_{0.5}\text{O}_2$.

4. Experimental Section

The $\text{Na}_{0.67}\text{Mn}_{0.5}\text{Fe}_{0.5}\text{O}_2$ composition was synthesized by modification of the conventional solid-state method by quenching the powder at high temperature. Appropriate amounts of reagent grade Na_2O_2 , Fe_2O_3 , and Mn_2O_3 were mixed in an agate mortar for 1 h in a glove box. The mixed

powders were heat treated in an $\alpha\text{-Al}_2\text{O}_3$ crucible at 1000 °C for 16 h under air and quenched in liquid nitrogen. After quenching, the samples were stored in the glove box.

The XRD patterns of samples were collected by a Rigaku RadB Dmax diffractometer with Cu K α ($\lambda_{\text{K}\alpha} = 1.5405 \text{ \AA}$) radiation. The GSAS-II open source program^[34] was used for Rietveld refinement^[35] to analyze the XRD data. FTIR spectra of samples were obtained by a Perkin Elmer, Spectrum One model between the range of 400 and 4000 cm^{-1} . The XAFS measurements were performed in the XRF/XAFS beamline at SESAME–Jordan. Microstructural characterization was performed with a Leo EVO-40 VPX SEM. Magnetic properties were investigated by a physical properties measurement system (PPMS) by Quantum Design.

To fabricate CR2032 cells, the active material, acetylene black, and polyvinylidene fluoride (70%:15%:15%) were mixed into slurries in *N*-methyl-2-pyrrolidone in an agate mortar and stirred with a magnetic stirrer for 24 h at room temperature. The mixture was coated onto aluminum foils by a micrometer adjustable film applicator blade and then dried at 110 °C for 10 h under vacuum condition. Discs (diameter 12 mm) of the coated films were punched and transferred to a glove box (Inert Technology, I-Lab) that was filled by spectroscopic argon gas. The amount of active materials in the CR2032 cells was $\approx 3.0\text{--}5.0 \text{ mg}$ on the Al foil. CR2032-type coin cells with pure Na metal as the counter electrode were assembled in the glove box using 1 M NaClO_4 in PC + 5% FEC electrolyte.

The CV measurements were performed between 1.5 and 4.0 V at a scan rate of 0.1 mV s^{-1} . An eight-channel battery analyzer system by Ivium Octostat30 was used for the galvanostatic charge/discharge measurements between 1.5 and 4.0 V at C/3 rate. To determine the environmental temperature dependence of the electrochemical properties between 10 and 50 °C, a Zive SP1 galvanostat/potentiostat system was integrated with a NUVE EN-120 incubator.

Acknowledgements

The authors would like to thank TUBITAK for the financial support by the contract number of 119M169. S.A. and S.A. would like to thank SESAME for XAS experiments with project numbers 20160053 and 20185100. S.A. and E.O. would like to thank the EU CALIPSOplus program and S.A. would like to thank the Turkish Atomic Energy Institute for travel support for XAS experiments. S.A. would like to acknowledge the financial support of the Istanbul Medeniyet University under project number F-GAP-2019-1498.

Conflict of Interest

The authors declare no conflict of interest.

Data Availability Statement

Data available on request from the authors.

Keywords

degradation mechanism, diffusion, Fourier transform infrared spectroscopy, $\text{Na}_{0.67}\text{Mn}_{0.5}\text{Fe}_{0.5}\text{O}_2$, X-ray absorption fine structure, X-ray diffraction

Received: December 28, 2020

Revised: February 25, 2021

Published online: March 31, 2021

[1] C. Delmas, C. Fouassier, P. Hagenmuller, *Phys. B+C* **1980**, 99, 81.

[2] J. K. Park, G. G. Park, H. H. Kwak, S.T. Hong, J. W. Lee, *ACS Omega* **2017**, 3, 361.

- [3] D. Kim, E. Lee, M. Slater, W. Lu, S. Rood, C. S. Johnson, *Electrochem. Commun.* **2012**, 18, 66.
- [4] C. Zhao, Y. Lu, L. Chen, Y. S. Hu, *Nano Res.* **2019**, 12, 2018.
- [5] E. Talaie, V. Duffort, H. L. Smith, B. Fultz, L. F. Nazar, *Energy Environ. Sci.* **2015**, 8, 2512.
- [6] N. Yabuuchi, M. Kajiyama, J. Iwatate, H. Nishikawa, S. Hitomi, R. Okuyama, R. Usui, Y. Yamada, S. Komaba, *Nat. Mater.* **2012**, 11, 512.
- [7] J. Wang, D. Zhou, X. He, L. Zhang, X. Cao, D. Ning, B. Yan, X. Qi, J. Li, V. Murzin, E. Paillard, X. Liu, G. Schumacher, M. Winter, J. Li, *ACS Appl. Mater. Interfaces* **2020**, 12, 5017.
- [8] D. Nayak, T. Sarkar, N. V. P. Chaudhary, M. D. Bhargadwaj, S. Ghosh, V. Adyam, *J. Solid State Electrochem.* **2018**, 22, 1079.
- [9] E. Altin, S. Altundag, S. Altin, A. Bayri, *J. Mater. Sci. Mater. Electron.* **2019**, 30, 17848.
- [10] J. Xu, S.-L. Chou, J.-L. Wang, H.-K. Liu, S.-X. Dou, *ChemElectroChem* **2014**, 1, 371.
- [11] K. J. Rao, H. Benqlilou-Moudden, B. Desbat, P. Vinatier, A. Levasseur, *J. Solid State Chem.* **2002**, 165, 42.
- [12] D. Danset, A. M. E. Alikhani, L. Manceron, *J. Phys. Chem. A* **2004**, 109, 97.
- [13] G. Gryn'ova, M. L. Coote, C. Corminboeuf, *Wiley Interdiscip. Rev. Comput. Mol. Sci.* **2015**, 5, 440.
- [14] H. Wang, R. Gao, Z. Li, L. Sun, Z. Hu, X. Liu, *Inorg. Chem.* **2018**, 57, 5249.
- [15] N. Ortiz-Vitoriano, N. E. Drewett, E. Gonzalo, T. Rojo, *Energy Environ. Sci.* **2017**, 10, 1051.
- [16] J. S. Chai, H. Tian, A. J. Mao, L. J. Deng, X. Y. Kuang, *RSC Adv.* **2016**, 6, 54041.
- [17] D. I. Khomskii, *Transition Metal Compounds*, Cambridge University Press, Cambridge **2014**.
- [18] H. Hafiz, K. Suzuki, B. Barbiellini, Y. Orikasa, S. Kaprzyk, N. Tsuji, K. Yamamoto, A. Terasaka, K. Hoshi, Y. Uchimoto, Y. Sakurai, H. Sakurai, A. Bansil, *Phys. Rev. B* **2019**, 100, 205104.
- [19] E. Oz, S. Demirel, S. Altin, E. Altin, A. Bayri, S. Avci, *Electrochim. Acta* **2017**, 248, 449.
- [20] N. Elgrishi, K. J. Rountree, B. D. McCarthy, E. S. Rountree, T. T. Eisenhart, J. L. Dempsey, *J. Chem. Educ.* **2018**, 95, 197.
- [21] L. Daniel, A. Bonakdarpour, D. P. Wilkinson, *ACS Appl. Nano Mater.* **2019**, 2, 3127.
- [22] Y. Bai, L. Zhao, C. Wu, H. Li, Y. Li, F. Wu, *ACS Appl. Mater. Interfaces* **2016**, 8, 2857.
- [23] M. H. Han, B. Acebedo, E. Gonzalo, P. S. Fontecoba, S. Clarke, D. Saurel, T. Rojo, *Electrochim. Acta* **2015**, 182, 1029.
- [24] M. Li, D. L. Wood, Y. Bai, R. Esseli, M. R. Amin, C. Jafra, N. Muralidharan, J. Li, I. Belharouak, *ACS Appl. Mater. Interfaces* **2020**, 12, 23951.
- [25] C. Qiu, G. He, W. Shi, M. Zou, C. Liu, *J. Solid State Electrochem.* **2019**, 23, 1887.
- [26] V. J. Ovejas, A. Cuadras, *J. Power Sources* **2019**, 418, 176.
- [27] B. Saha, P. Quach, K. Goebel, presented at *Annual Conf. of the Prognostics and Health Management Society*, Montreal, Quebec, Canada, September **2011**.
- [28] X. Zhu, L. Wang, *EcoMat* **2020**, 2, e12043.
- [29] E. Marelli, C. Villeveille, S. Park, N. Hérault, C. Marino, *ACS Appl. Energy Mater.* **2018**, 1, 5960.
- [30] Sigma-Aldrich, Whatman® glass microfiber filters, <https://www.sigmaaldrich.com> (accessed: March 2019).
- [31] M. Diantoro, D. N. Prastivi, A. Taufiq, N. Hidayat, N. Mufti, A. Hidayat, *J. Phys. Conf. Ser.* **2017**, 846, 012007.
- [32] J. Zhu, Q. Li, Y. Che, X. Liu, C. Dong, X. Chen, C. Wang, *Polymers* **2020**, 12, 453.
- [33] F. Wang, F. Varenne, D. Ortiz, V. Pinzio, M. Mostafavi, S. Le Caër, *ChemPhysChem* **2017**, 18, 2799.
- [34] B. H. Toby, R. B. Von Dreele, *IUCr, J. Appl. Crystallogr.* **2013**, 46, 544.
- [35] H. M. Rietveld, *J. Appl. Crystallogr.* **1969**, 2, 65.
- [36] V. T. Le, T. M. Pham, V. D. Doan, O. E. Lebedeva, H. T. Nguyen, *Sep. Sci. Technol.* **2019**, 54, 3070.
- [37] V. G. P. Ribeiro, A. C. H. Barreto, J. C. Denardin, G. Mele, L. Carbone, S. E. Mazzetto, E. M. B. Sousa, P. B. A. Fechine, *J. Mater. Sci.* **2013**, 48, 7875.
- [38] S. Musi, I. Nowik, M. Risti, Z. Orehovec, S. Popovi, *Croat. Chem. Acta* **2004**, 77, 141.
- [39] J. Liang, D. Wei, Q. Cheng, Y. Zhu, X. Li, L. Fan, J. Zhang, Y. Qian, *ChemPlusChem* **2014**, 79, 143.
- [40] L. Ren, H. Qiu, W. Qin, M. Zhang, Y. Li, P. Wei, *R. Soc. Open Sci.* **2018**, 5, 100158.
- [41] A. Yuan, X. Wang, Y. Wang, J. Hu, *Electrochim. Acta* **2009**, 54, 1021.
- [42] F. Ahangaran, A. Hassanzadeh, S. Nouri, *Int. Nano Lett.* **2013**, 3, 1.
- [43] J. K. Kumar, A. G. Devi Prasad, *Rom. J. Biophys.* **2011**, 21, 63.
- [44] F. Ardelean, E. A. Moaca, C. Pacurariu, D. S. Antal, C. Dehelean, C. C. Toma, S. Dragan, *Studia Univ. Vasile Goldis* **2016**, 26, 415.
- [45] B. Douzandeh-Mobarrez, M. Ansari-Dogaheh, T. Eslaminejad, M. Kazempour, M. Shakibaie, *Iran. J. Biotechnol.* **2018**, 16, 287.
- [46] C. D. S. Peretiatko, E. A. Hupalo, J. R. da R. Campos, C. R. B. Parabocz, *Orbital* **2018**, 10, 218.
- [47] V. B. Borugadda, V. V. Goud, *Tribol. Online* **2015**, 10, 354.
- [48] S. P. Lee, N. Mellon, A. M. Shariff, J. M. Leveque, *IOP Conf. Ser. Mater. Sci. Eng.* **2017**, 226, 012173.
- [49] D. B. Priya, I. V. Asharani, *IET Nanobiotechnol.* **2018**, 12, 116.
- [50] L. Yang, P. W. May, L. Yin, J. A. Smith, K. N. Rosser, *J. Nanoparticle Res.* **2007**, 9, 1181.
- [51] J. Li, D. Liu, B. Li, J. Wang, S. Han, L. Liu, H. Wei, *CrystEngComm* **2015**, 17, 520.
- [52] I. Y. Abdullah, M. Yahaya, M. H. H. Jumali, H. M. Shanshool, *Am. Inst. Phys. Conf. Proc.* **2014**, 1614, 147.
- [53] X. Lu, Y. Peng, H. Qiu, X. Liu, L. Ge, *Desalination* **2017**, 413, 127.
- [54] Y. Chen, K. Zhang, F. Yuan, T. Zhang, B. Weng, S. Wu, A. Huang, N. Su, Y. Guo, *Materials* **2018**, 11, 541.
- [55] S. T. C. L. Ndruru, D. Wahyuningrum, B. Bundjali, I. M. Arcana, *IOP Conf. Ser. Mater. Sci. Eng.* **2019**, 541, 012017.
- [56] H. M. Yang, H. J. Lee, K. S. Jang, C. W. Park, H. W. Yang, W. Do Heo, J. D. Kim, *J. Mater. Chem.* **2009**, 19, 4566.
- [57] T. Vijayaraghavan, R. Sivasubramanian, S. Hussain, A. Ashok, *ChemistrySelect* **2017**, 2, 5570.
- [58] Y.-M. Zhang, X.-M. You, H. Yao, Y. Guo, P. Zhang, B.-B. Shi, J. Liu, Q. Lin, T.-B. Wei, *Supramol. Chem.* **2014**, 26, 39.
- [59] N. Rangelova, L. Radev, S. Nenkov, I. M. M. Salvado, M. H. V. Fernandes, M. Herzog, *Cent. Eur. J. Chem.* **2011**, 9, 112.
- [60] E. W. Lemmon, M. O. McLinden, D. G. Friend, NIST Chemistry WebBook, <https://webbook.nist.gov/chemistry> (accessed: March 2019).
- [61] N. Can, A. Ataç, F. Bardak, Ş. E. S. Can, *Turkish J. Chem.* **2005**, 29, 589.
- [62] M. Santoro, F. A. Gorelli, R. Bini, J. Haines, A. Van Der Lee, *Nat. Commun.* **2013**, 4, 1.
- [63] M. K. Trivedi, A. B. Dahryn Trivedi, H. S. Khemraj Bairwa, *Nat. Prod. Chem. Res.* **2015**, 3, 1000186.
- [64] Y. Chen, Y. H. Zhang, L. J. Zhao, *Phys. Chem. Chem. Phys.* **2004**, 6, 537.
- [65] R. Senthil Kumar, P. Rajkumar, *Atmos. Chem. Phys. Discuss.* **2013**, 13, 22221.
- [66] J. T. Klopogge, R. D. Schuiling, Z. Ding, L. Hickey, D. Wharton, R. L. Frost, *Vib. Spectrosc.* **2002**, 28, 209.